

The inner workings of the hydrazine synthase multiprotein complex

Andreas Dietl¹, Christina Ferousi², Wouter J. Maalcke², Andreas Menzel³, Simon de Vries^{4,†}, Jan T. Keltjens², Mike S. M. Jetten^{2,4}, Boran Kartal^{2,5} & Thomas R. M. Barends¹

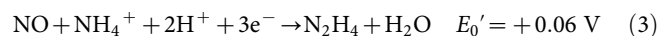
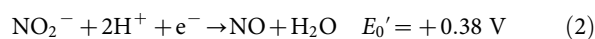
Anaerobic ammonium oxidation (anammox) has a major role in the Earth's nitrogen cycle^{1,2} and is used in energy-efficient wastewater treatment³. This bacterial process combines nitrite and ammonium to form dinitrogen (N₂) gas, and has been estimated to synthesize up to 50% of the dinitrogen gas emitted into our atmosphere from the oceans². Strikingly, the anammox process relies on the highly unusual, extremely reactive intermediate hydrazine⁴, a compound also used as a rocket fuel because of its high reducing power. So far, the enzymatic mechanism by which hydrazine is synthesized is unknown. Here we report the 2.7 Å resolution crystal structure, as well as biophysical and spectroscopic studies, of a hydrazine synthase multiprotein complex isolated from the anammox organism *Kuenenia stuttgartiensis*. The structure shows an elongated dimer of heterotrimers, each of which has two unique *c*-type haem-containing active sites, as well as an interaction point for a redox partner. Furthermore, a system of tunnels connects these active sites. The crystal structure implies a two-step mechanism for hydrazine synthesis: a three-electron reduction of nitric oxide to hydroxylamine at the active site of the γ -subunit and its subsequent condensation with ammonia, yielding hydrazine in the active centre of the α -subunit. Our results provide the first, to our knowledge, detailed structural insight into the mechanism of biological hydrazine synthesis, which is of major significance for our understanding of the conversion of nitrogenous compounds in nature.

Most nitrogen on earth occurs as gaseous N₂ (nitrogen oxidation number 0). To make nitrogen available for biochemical reactions, the inert N₂ has to be converted to ammonia (oxidation number -III), which can then be assimilated to produce organic nitrogen compounds, or be oxidized to nitrite (oxidation number +III) or nitrate (+V). The reduction of nitrite in turn results in the regeneration of N₂, thus closing the biological nitrogen cycle.

To produce N₂ from nitrite, a nitrogen–nitrogen bond must be formed by the addition of another nitrogen-containing molecule. At present, two biological processes are known that can achieve this. In denitrification, nitrite is first reduced to nitric oxide (NO, +II). Then, two molecules of NO are combined to produce nitrous oxide (N₂O, +I), which is subsequently reduced to N₂. The other process, anaerobic ammonium oxidation or anammox^{1,2}, was discovered only relatively recently, and relies on the combination of two compounds with different nitrogen oxidation states, nitrite and ammonium, to generate N₂.

Our current understanding of the anammox reaction (equation (1)) is based on genomic, physiological and biochemical studies on the anammox bacterium *K. stuttgartiensis*^{4,5}. First, nitrite is reduced to nitric oxide (NO, equation (2)), which is then condensed with ammonium-derived ammonia (NH₃) to yield hydrazine (N₂H₄, equation (3)). Hydrazine itself is a highly unusual metabolic intermediate, as it is extremely reactive and therefore toxic, and has a very low redox poten-

tial ($E_0' = -750$ mV). In the final step in the anammox process, it is oxidized to N₂, yielding four electrons (equation (4)) that replenish those needed for nitrite reduction and hydrazine synthesis and are used to establish a proton-motive force across the membrane of the anammox organelle, the anammoxosome, driving ATP synthesis (see ref. 6 for a review).



The enzyme producing hydrazine from NO and ammonium—hydrazine synthase (HZS)—is biochemically unique. A complex of three proteins, HZS- α , - β and - γ , encoded by the genes *kuste2861*, *-2859* and *-2860*, respectively, was put forward as the probable hydrazine synthase enzyme⁵. This complex was isolated from *K. stuttgartiensis* cells and shown to be catalytically active in a coupled assay with the octahaem *c*-type cytochrome *kustc1061* (ref. 7) to convert hydrazine into N₂ and return electrons to HZS⁴. Isolated HZS is a comparatively slow enzyme with an activity of 20 nmol h⁻¹ mg⁻¹ protein, about 1% of *in vivo* turnover. This striking loss of activity occurs immediately upon cell lysis and might be explained by the disruption of a tightly coupled multicomponent system, as well as by the use of bovine cytochrome *c* as an artificial electron carrier in the *in vitro* assay⁴.

Using a custom-designed crystal cooling method, we prepared well-diffracting crystals of the HZS- $\alpha\beta\gamma$ multienzyme complex from *K. stuttgartiensis* and determined its crystal structure at 2.7 Å resolution in the absence of substrates (Fig. 1a and Extended Data Table 1). The structure reveals a crescent-shaped dimer of heterotrimers with an ($\alpha\beta\gamma$)₂ stoichiometry. The overall size and shape of the complex were confirmed by analytical ultracentrifugation and solution small-angle X-ray scattering (Supplementary Information and Extended Data Fig. 1). Each heterotrimer contains four haems and one zinc ion, as well as several calcium ions (Fig. 1b, Supplementary Information and Extended Data Table 2).

The α -subunit (Fig. 1c) consists of three domains: an N-terminal domain which includes a six-bladed β -propeller, a middle domain binding a pentacoordinated *c*-type haem (αI) and a C-terminal domain which harbours a bis-histidine-coordinated *c*-type haem (αII). The structure around haem αI (Fig. 1d) deviates substantially from a typical haem *c* site, as the canonical histidine of the haem *c* binding motif, αHis587 , is rotated away from the haem iron, and coordinates a zinc ion. Instead, the hydroxyl group of αTyr591 serves as the proximal ligand to the haem iron, as in the active site of

¹Department of Biomolecular Mechanisms, Max Planck Institute for Medical Research, 69120 Heidelberg, Germany. ²Department of Microbiology, Institute for Water and Wetland Research, Radboud University Nijmegen, 6525 AJ Nijmegen, The Netherlands. ³Swiss Light Source, Paul Scherrer Institute, 5232 Villigen, Switzerland. ⁴Department of Biotechnology, Delft University of Technology, Delft, The Netherlands. ⁵Department of Biochemistry and Microbiology, Laboratory of Microbiology, Gent University, Gent, Belgium.

†Deceased.

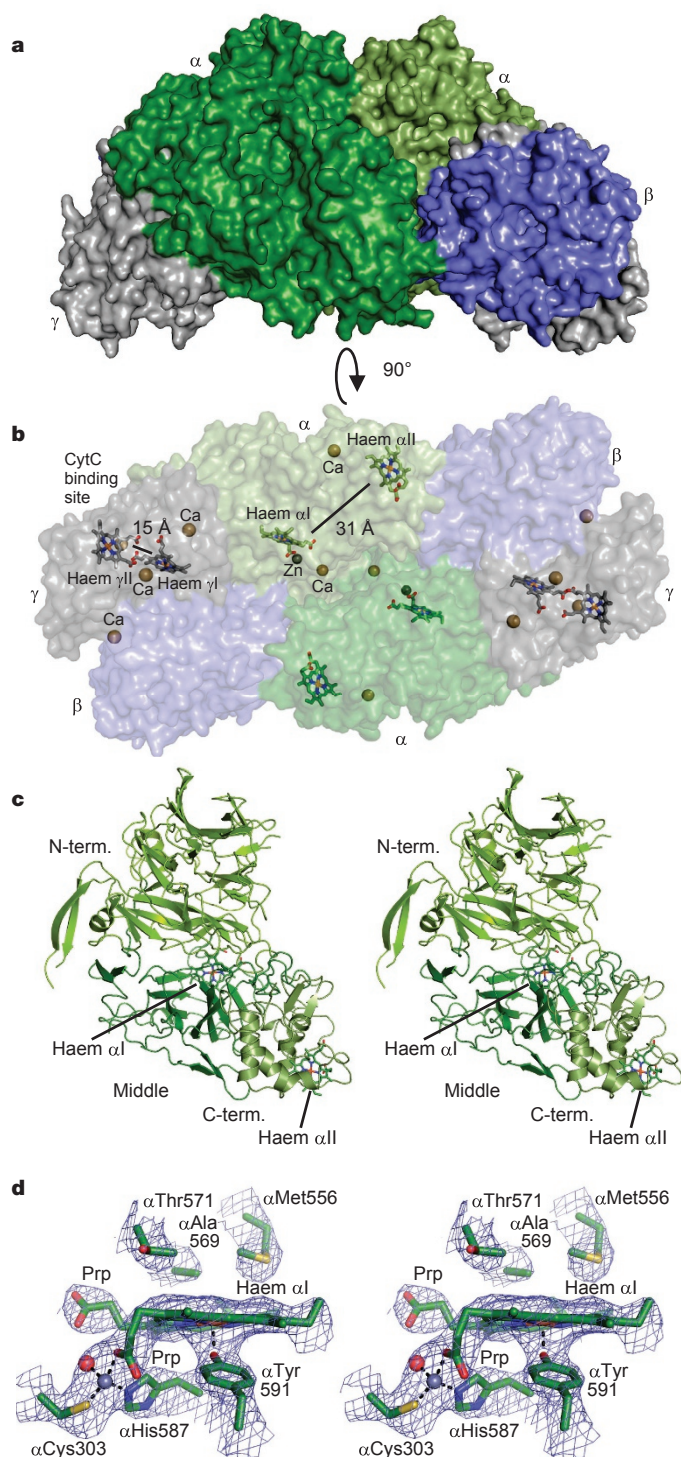


Figure 1 | Crystal structure of HZS. **a**, HZS complex structure; α -subunits are coloured green, β -subunits are blue and γ -subunits are grey. **b**, Surface representation. The contact area between two heterotrimers ($\sim 1,350 \text{ \AA}^2$) is made up of contributions from α - and β -subunits only. Considerable solvent-filled space remains between the heterotrimers. Calcium ions are labelled Ca, zinc as Zn. Edge-to-edge distances between the haems within a subunit are indicated in ångströms. **c**, Stereofigure of the α -subunit. The N-terminal domain (residues $\alpha 28$ – 420), middle domain ($\alpha 421$ – $\alpha 670$) and C-terminal domain ($\alpha 671$ – 808) are indicated in different shades of green. The two haem groups are shown as sticks. **d**, Stereofigure of the haem α I site, overlaid with the simulated annealing composite omit map, contoured at 1.0σ . The zinc ion and its coordinating water are shown as grey and red spheres, respectively. The haem propionates are labelled Prp.

many catalases⁸. Importantly, this tyrosine is conserved in HZS- α sequences (Extended Data Fig. 2). The zinc bound to α His587 is further coordinated by one of the haem α I propionate groups, as well as α Cys303 and probably a water molecule, in a structure reminiscent of the active sites of alcohol dehydrogenase and various metalloproteases⁹. The zinc ion could play a structural role, assisting in rotating α His587 away from the iron, allowing α Tyr591 to bind, or could directly modulate the chemistry of the haem group, with which it interacts via a propionate group. α Thr571, α Ala569 and α Met556 (which is partially oxidized, see Supplementary Information) are in close proximity to the distal side of haem α I, which does not seem to coordinate a solvent molecule in the crystal structure. In contrast, haem α II is bound by a canonical haem *c* binding motif and is coordinated by α His772 distally and α His689 proximally. The edge-to-edge distance¹⁰ between haems α I and α II is 31 \AA (Fig. 1b), which is too long for single-step electron transfer between the haem groups of the α -subunit. The edge-to-edge distances between the haem groups in the two different α -subunits in the complex are larger than 38 \AA , which excludes electron transfer between the two α -subunits on the timescale of catalysis.

The non-haem β -subunit (Fig. 2a) is a seven-bladed β -propeller with a short helical insertion in the sixth propeller blade. The outer strand of the C-terminal blade consists of the N terminus (residues $\gamma 40$ – 52) of the γ -subunit of the same heterotrimer. Notably, the HZS β - and γ -subunits are fused into a single polypeptide in the anammox bacteria *Scalindua profunda* and *Scalindua brodae* (ref. 11 and Extended Data Fig. 3).

The structure of the γ -subunit (Fig. 2b) is reminiscent of the fold of the homologous dihaem cytochrome *c* peroxidases (CCPs)^{12–14} and *Paracoccus denitrificans* methylamine utilization protein G (MauG)¹⁵ and consists of two α -helical lobes, each of which contains one *c*-type haem. Haem γ I in the N-terminal lobe (Fig. 2c) is coordinated proximally by γ His106 and distally by a water molecule, and is covalently bound to γ Cys102 and γ Cys105 on a typical haem *c* binding motif. Intriguingly, the electron density maps clearly show a unique third covalent bond with the protein, between the C_1 porphyrin methyl group and the S_γ sulfur atom of γ Cys165 (Extended Data Fig. 4a), which possibly serves to modulate haem chemistry. At the distal side, the iron binds a water molecule, which is hydrogen bonded to γ Asp168. This conserved residue (Extended Data Fig. 3) is perfectly positioned to transfer protons to a ligand molecule coordinated to the haem. A structural superposition (Extended Data Fig. 4b) reveals that haem γ I is located at the position of the high-spin haem of the homologous *Nitrosomonas europaea* CCP¹³ and *P. denitrificans* MauG¹⁵.

The bis-His-coordinated haem γ II in the C-terminal lobe is located at the equivalent position as the electron transfer haem in CCPs and MauG (Extended Data Fig. 4b), at an edge-to-edge distance of 15 \AA from haem γ I (Fig. 1b), which would allow direct electron transfer between the haems in the γ -subunit. In CCPs and MauG, a conserved Trp residue is believed to be involved in catalytic redox chemistry. In HZS- γ , the position of this tryptophan is taken up by γ His144. The γ -subunit binds three calcium ions, one of them at the same position as the Ca-binding site in CCP that is essential for its activation. Moreover, haem γ II is located on the surface of the complex, exposed to the solvent, surrounded by a negatively charged patch, as in a cytochrome *c* binding site (Extended Data Fig. 5). Therefore, haem γ II probably functions in electron transfer.

Thus, it appears that the α - and the γ -subunit each contain an active site (haems α I and γ I) and the γ -subunit contains an electron-transfer site (haem γ II). Electron paramagnetic resonance (EPR) spectroscopy (Extended Data Fig. 6 and Supplementary Information) is consistent with a stoichiometry of two bis-His-coordinated haems and two haems for which a population of ligation states exist.

Intriguingly, our crystal structure revealed a tunnel connecting the haem α I and γ I sites (Fig. 3a). This tunnel branches off towards the surface of the protein approximately halfway between the haem sites,

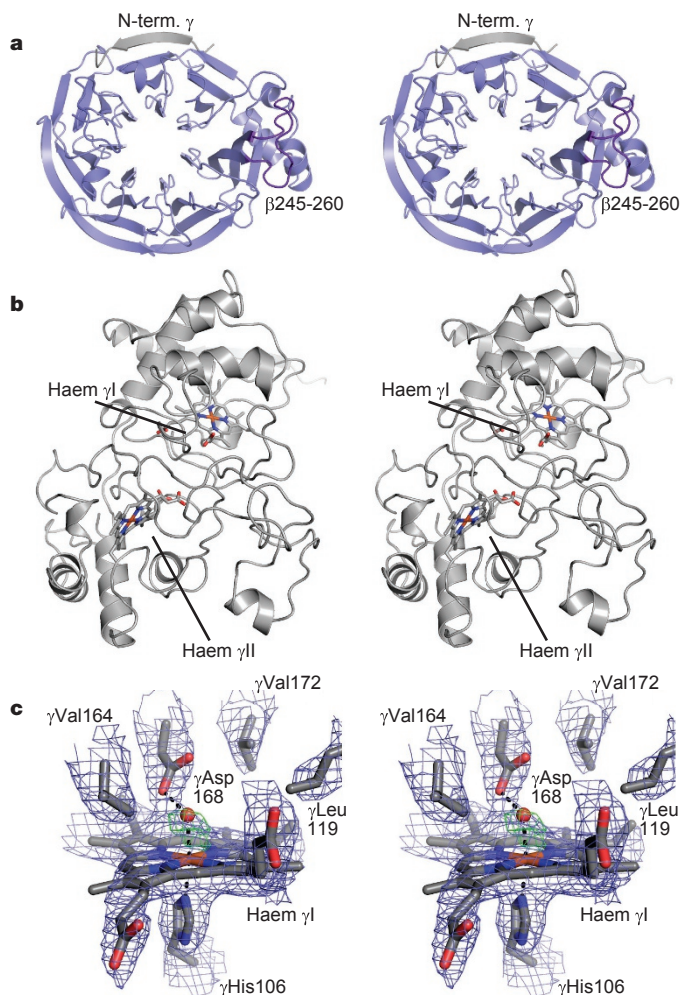
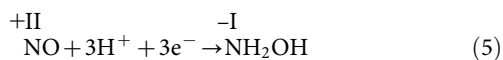


Figure 2 | Structure of HZS- β and HZS- γ . **a**, Structure of the β -subunit. The β 245–260 insertion is shown in purple. The N terminus of the γ -subunit, which engages in β -completion with the first blade of the β -propeller is shown in grey. **b**, Structure of the γ -subunit. **c**, Stereofigure of haem γ I and its surroundings, overlaid with the simulated annealing composite omit map (blue, 1.0σ). The water molecule bound to the haem iron is shown as a red sphere. The green mesh is the difference electron density calculated before inclusion of the water molecule in the model (5.0σ).

making them accessible to substrates from the solvent. Indeed, binding studies show that haem α I is accessible to xenon (Extended Data Fig. 4c). Interestingly, in-between the α - and γ -subunits, the tunnel is approached by a 15-amino-acid-long loop of the β -subunit (β 245–260), placing the conserved β Glu253, which binds a magnesium ion, into the tunnel.

These observations allow a mechanism for biological hydrazine synthesis to be proposed (Fig. 3b). The presence of two active sites, connected by a tunnel, strongly suggests a mechanism with two half-reactions. HZS combines NO (nitrogen oxidation number +II) and NH_4^+ (N oxidation number –III). To reach the –II oxidation number of the nitrogen atoms in hydrazine, nitric oxide must be reduced. As proposed earlier⁶, this could happen in the γ -subunit, resulting in the production of hydroxylamine (NH_2OH ; nitrogen oxidation number –I) according to equation (5).



This three-electron reduction is consistent with the proposal that HZS obtains electrons from the trihaem cytochrome *c* kuste2854 (ref. 6). In this scheme, the electrons would enter HZS through haem γ II and be

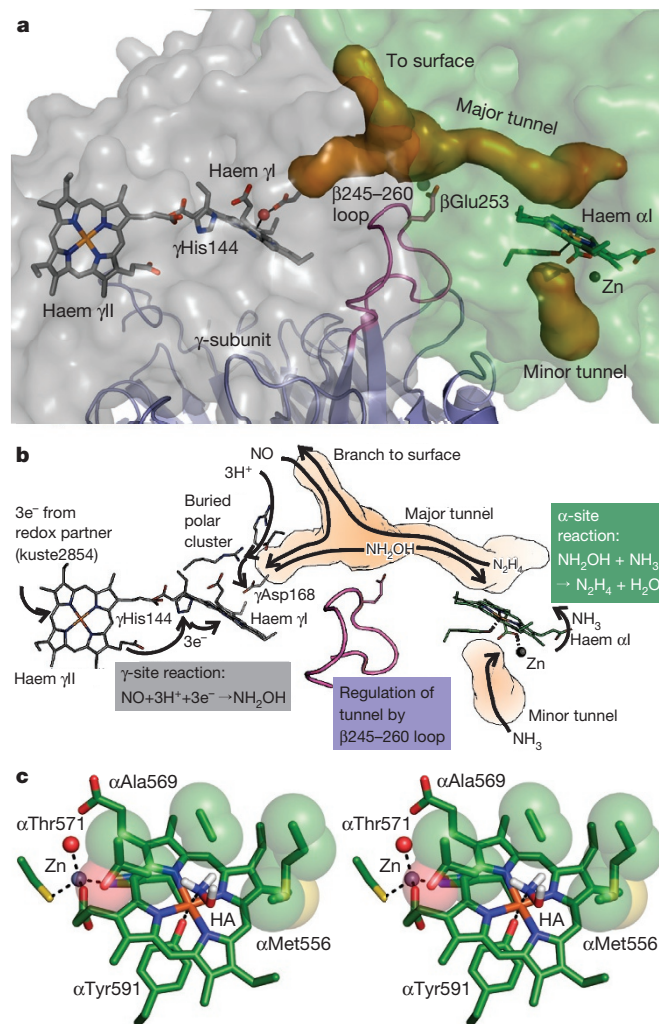
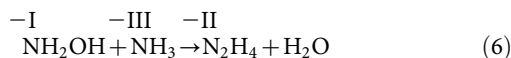


Figure 3 | Proposed mechanism of biological hydrazine synthesis. **a**, Tunnel between the active site haems (orange, major tunnel) with the branch to the protein surface. The β 245–260 loop is shown in purple, as well as β Glu253 which binds a magnesium ion (light-green sphere) and γ His144. A minor tunnel (lower right) leads to the zinc ion, and could allow ammonium to enter. **b**, Details of the proposed mechanism. NO travels to haem γ I through the tunnel (orange) via the branch leading to the surface. On the left, three electrons enter the complex at haem γ II and are conducted to haem γ I via γ His144. Together with three protons reaching haem γ I from the solvent via the buried polar cluster, the electrons reduce NO to NH_2OH (grey box). NH_2OH then diffuses through the tunnel, which is regulated by the β -subunit through the β 245–260 loop, and binds to haem α I. There, it undergoes comproportionation with NH_3 to yield hydrazine (green box). **c**, Stereofigure, showing a model of hydroxylamine (HA) bound to haem α I in a very hydrophobic environment.

transferred to the active site haem γ I, possibly via γ His144. γ Asp168 could assist in adding the protons. A cluster of buried, polar residues (γ Asp112, γ Arg143 and γ Arg167) is positioned between γ Asp168 and the surface of the complex and could serve to transfer protons to the active centre of the γ -subunit.

In the proposed mechanism, hydroxylamine then diffuses through the tunnel to the α -subunit's active site. Given the position of the β 245–260 loop, the β -subunit could play a role in modulating transport through the tunnel. Hydroxylamine is isoelectronic with hydrogen peroxide, and is a competitive catalase inhibitor¹⁶. Thus, it would bind to the distal coordination site of the catalase-like haem α I, which would polarize the N–O bond. As crystal soaking with NH_2OH was unsuccessful, we constructed a model of this complex

(Fig. 3c) which shows that hydroxylamine would be bound in a tight, very hydrophobic pocket, so that there is little electrostatic shielding of the partial positive charge on the nitrogen. Ammonia produced from ammonium (the predominant form at pH = 6.3 in the anammoxosome¹⁷) could then perform a nucleophilic attack on the nitrogen of hydroxylamine, yielding hydrazine through comproportionation (equation (6)).



Hydrazine could leave the enzyme via the tunnel branch leading to the surface.

Interestingly, the proposed scheme is analogous to the Raschig process used in industrial hydrazine synthesis. There, ammonia is oxidized to chloramine (NH₂Cl, nitrogen oxidation number –I, like in hydroxylamine), which then undergoes comproportionation with another molecule of ammonia to yield hydrazine.

Online Content Methods, along with any additional Extended Data display items and Source Data, are available in the online version of the paper; references unique to these sections appear only in the online paper.

Received 1 April; accepted 21 August 2015.

Published online 19 October 2015.

1. Devol, A. H. Denitrification, anammox, and N₂ production in marine sediments. *Ann. Rev. Mar. Sci.* **7**, 403–423 (2015).
2. Lam, P. & Kuypers, M. M. M. Microbial nitrogen cycling processes in oxygen minimum zones. *Ann. Rev. Mar. Sci.* **3**, 317–345 (2011).
3. Kartal, B., Kuenen, J. G. & van Loosdrecht, M. C. M. Sewage treatment with anammox. *Science* **328**, 702–703 (2010).
4. Kartal, B. *et al.* Molecular mechanism of anaerobic ammonium oxidation. *Nature* **479**, 127–130 (2011).
5. Strous, M. *et al.* Deciphering the evolution and metabolism of an anammox bacterium from a community genome. *Nature* **440**, 790–794 (2006).
6. Kartal, B. *et al.* How to make a living from anaerobic ammonium oxidation. *FEMS Microbiol. Rev.* **37**, 428–461 (2013).
7. Maalcke, W. J. *et al.* Structural basis of biological NO generation by octaheme oxidoreductases. *J. Biol. Chem.* **289**, 1228–1242 (2014).
8. Putnam, C. D., Arvai, A. S., Bourne, Y. & Tainer, J. A. Active and inhibited human catalase structures: ligand and NADPH binding and catalytic mechanism. *J. Mol. Biol.* **296**, 295–309 (2000).
9. Auld, D. S. Zinc coordination sphere in biochemical zinc sites. *Biometals* **14**, 271–313 (2001).
10. Moser, C. C., Chobot, S., Page, C. & Dutton, L. Distance metrics for heme protein electron tunneling. *Biochim. Biophys. Acta* **1777**, 1032–1037 (2008).

11. van de Vossenberg, J. *et al.* The metagenome of the marine anammox bacterium ‘*Candidatus Scalindua profunda*’ illustrates the versatility of this globally important nitrogen cycle bacterium. *Environ. Microbiol.* **15**, 1275–1289 (2013).
12. Fülöp, V., Ridout, C. J., Greenwood, C. & Hajdu, J. Crystal structure of the di-heme cytochrome c peroxidase from *Pseudomonas aeruginosa*. *Structure* **3**, 1225–1233 (1995).
13. Shimizu, H. *et al.* Crystal structure of *Nitrosomonas europaea* cytochrome c peroxidase and the structural basis for ligand switching in bacterial di-heme peroxidases. *Biochemistry* **40**, 13483–13490 (2001).
14. Echalié, A. *et al.* Redox-linked structural changes associated with the formation of a catalytically competent form of the di-heme cytochrome c peroxidase from *Pseudomonas aeruginosa*. *Biochemistry* **47**, 1947–1956 (2008).
15. Jensen, L. M. R., Sanishvili, R., Davidson, V. L. & Wilmot, C. M. In crystallo posttranslational modification within a MauG/Pre-methylamine dehydrogenase complex. *Science* **327**, 1392–1394 (2010).
16. Blaschko, H. The mechanism of catalase inhibitions. *Biochem. J.* **29**, 2303–2312 (1935).
17. van der Star, W. R. L. *et al.* An intracellular pH gradient in the anammox bacterium *Kuenea stuttgartiensis* as evaluated by ³¹P NMR. *Appl. Microbiol. Biotechnol.* **86**, 311–317 (2010).

Supplementary Information is available in the online version of the paper.

Acknowledgements We dedicate this work to Simon de Vries, who passed away unexpectedly shortly before the publication of this paper. The Dortmund-Heidelberg data collection team and the staff of beamline X10SA at the Swiss Light Source of the PSI in Villigen, Switzerland are acknowledged for their help and facilities. M. Gradl and M. Müller are thanked for assistance with MALDI- and ESI-TOF mass spectrometric analyses. We thank I. Schlichting, J. Reimann, M. Cryle, J. Reinstein and R. Shoeman for suggestions and C. Kieser (electronics workshop at MPIImF) for constructing the Peltier cooling controller used in post-crystallization treatment. T.R.M.B. thanks I. Schlichting for continuous support. B.K. and W.J.M. were supported by the Netherlands Organization for Scientific Research (VENI grant 863.11.003 and Darwin grant 142.16.1201, respectively). C.F. and M.S.M.J. are supported by the European Research Council (ERC232937) and by a Spinoza Prize awarded to M.S.M.J. Chimera is developed by the Resource for Biocomputing, Visualization, and Informatics at the University of California, San Francisco (supported by NIGMS P41-GM103311). This work was supported by the Max Planck Society.

Author Contributions C.F. and W.J.M. isolated the Kuste2859-60-61 complex from *K. stuttgartiensis*. A.D. and T.R.M.B. performed X-ray crystallographic, SAXS and AUC analyses. A.M. performed SAXS measurements. C.F. performed ICP-MS analyses. W.J.M. and S.deV. performed EPR sample preparation and analysis. A.D. and T.R.M.B. wrote the paper with input from M.S.M.J., J.T.K., S.deV., C.F., W.M. and B.K.

Author Information The atomic coordinates and structure factors have been deposited in the Protein Data Bank, under accession codes 5C2V and 5C2W. Reprints and permissions information is available at www.nature.com/reprints. The authors declare no competing financial interests. Readers are welcome to comment on the online version of the paper. Correspondence and requests for materials should be addressed to T.R.M.B. (Thomas.Barends@mpimf-heidelberg.mpg.de) or B.K. (kartal@science.ru.nl).

METHODS

Protein purification. The kuste2859-2860-2861 hydrazine synthase (HZS) complex was purified from a planktonic *K. stuttgartiensis* culture as described previously⁴. Briefly, cell-free extracts prepared from a ~95% single-cell enrichment culture of *K. stuttgartiensis* were subjected to ultracentrifugation (180,000g; 4 °C; 1 h) to pellet cell membranes. HZS present in the bright-red supernatant was brought to homogeneity by a two-step column purification procedure consisting of subsequent Q Sepharose XL (GE Healthcare) and CHT Ceramic Hydroxyapatite (Bio-Rad, USA) column chromatography steps. UV-Vis spectra of as-isolated HZS showed a Soret absorption peak at 406 nm and a broad band in the 530 nm region, which are typical for fully oxidized (ferric) haem *c* proteins. Reduction of the protein under anoxic conditions using sodium dithionite resulted in a shift of the Soret maximum to 420 nm as well as haem α - and β -bands at 553 nm and 523 nm, respectively. Protein concentrations used for ICP-MS and EPR measurements were determined using the Bradford assay (Bio-Rad, USA) with bovine serum albumin as standard.

Analyses by MALDI-TOF and ESI-TOF mass spectrometry. The subunits of the HZS complex were separated by 15% sodium dodecylsulfate polyacrylamide gel electrophoresis (SDS-PAGE). To identify the individual subunits of the HZS complex, Coomassie-stained SDS gel slices were digested with trypsin or chymotrypsin, followed by reduction with DTT and alkylation with iodoacetamide. The resulting peptides were purified and concentrated using a Millipore ZipTip C-18 column, spotted onto solid targets with α -cyanocinnamic acid, and analysed by matrix-assisted laser desorption/ionization time-of-flight mass spectrometry (MALDI-TOF MS) on an Axima TOP² Performance mass spectrometer (Shimadzu Biotech, Duisburg, Germany). Signal peptide cleavage sites were predicted using the SignalP 3.0 Server¹⁸ applying Hidden-Markov models for Gram-negative bacteria. Liquid HZS samples were analysed by electrospray ionization time-of-flight mass spectrometry (ESI-TOF MS) on a maXis spectrometer (Bruker Daltonics) under denaturing conditions after diluting in 50% (v/v) acetonitrile/0.1% formic acid and separation by reversed-phase high-performance liquid chromatography (RP-HPLC) using a Discovery BIO Wide Pore C5 column (20 × 2.1 mm, 5 μ m particle size, Supelco) at a flow rate of 50 μ l min⁻¹.

Metal analysis by inductively-coupled plasma mass spectrometry (ICP-MS). Metals were analysed by ICP-MS on a Series I ICP MS (Thermo Scientific, Breda, the Netherlands). Height point calibration was performed with a dilution series of (multi-) element standards (1,000 p.p.b. in 1% nitric acid; Merck, Darmstadt, Germany) using the PlasmaLab software (Thermo Scientific, Breda, the Netherlands). To determine the metal content of HZS, 70–300 μ l of purified HZS (26 mg protein per ml) was washed with water using a Vivaspin 500 filter (Sartorius, Göttingen, Germany), destructed with 10% nitric acid at 90 °C for 90 min and diluted to 10 ml with water.

Analytical ultracentrifugation (AUC). Protein samples were concentrated in 25 mM Hepes/KOH, pH 7.5, 25 mM KCl to $A_{280}^{1\text{cm}} \approx 0.3$ and $A_{406}^{1\text{cm}} \approx 0.45$, corresponding to 0.3 mg ml⁻¹, as determined using the Bradford protein assay from Bio-Rad. Sedimentation velocity analytical ultracentrifugation was performed in a Beckman ProteomeLab XL-I (Beckmann Coulter, Krefeld, Germany) analytical ultracentrifuge equipped with an An60Ti rotor at 30,000 r.p.m. and 20 °C in a two-sector cell with a 1.2 cm optical path length. Absorption scan data were collected at 280 nm and 406 nm and evaluated using SEDFIT¹⁹.

Protein crystallization and crystal treatment. Hydrazine synthase was concentrated to 45 mg ml⁻¹ in 25 mM HEPES/KOH pH 7.5, 25 mM KCl by ultrafiltration, divided into 50- μ l aliquots, frozen in liquid nitrogen and stored at -80 °C. Prior to crystallization, the protein stock was diluted to 30 mg ml⁻¹ with 25 mM HEPES/KOH pH 7.5, 25 mM KCl. Crystallization was performed in 1 μ l + 1 μ l sitting drop vapour-diffusion setups at 8 °C, equilibrating against 500 μ l 36% (v/v) 1,4-dioxane. Dark red, rhombohedral crystals with dimensions up to 400 × 400 × 100 μ m grew within three days. The addition of 1 mM 5-amino-2,4,6-triiodoisophthalic acid adjusted to pH 7 with ethanolamine to the precipitant solution in the drops yielded more crystals and accelerated crystal growth. Using PEG 400 or other conventional cryoprotectants, diffraction of these crystals suffered from diffuse scattering, limiting resolution to approx. 4 Å and precluding SAD phasing. Successful cryoprotection was carried out by soaking the crystals for 10–30 s in 4 M betaine (*N,N,N*-trimethylglycine) in 50% (v/v) methanol at 8 °C, before flash-cooling in liquid nitrogen. These crystals showed sharp Bragg spots, were used for phasing and to build the initial model. However, as the crystals dissolved in the soaking solution at 8 °C, crystals were slowly cooled to -20 °C on a custom-designed Peltier-cooled microscope stage, which will be described in detail elsewhere. After incubation in the soaking solution at this temperature for up to 30 min, crystals were flash-cooled in liquid propane at a temperature of approximately 150 K. These crystals diffracted up to 2.7 Å resolution. Xenon treatment was performed in a -20 °C room by transferring the crystals cooled to -20 °C into a Xe-pressure cell (Xcell, Oxford Cryosystems Ltd, Long

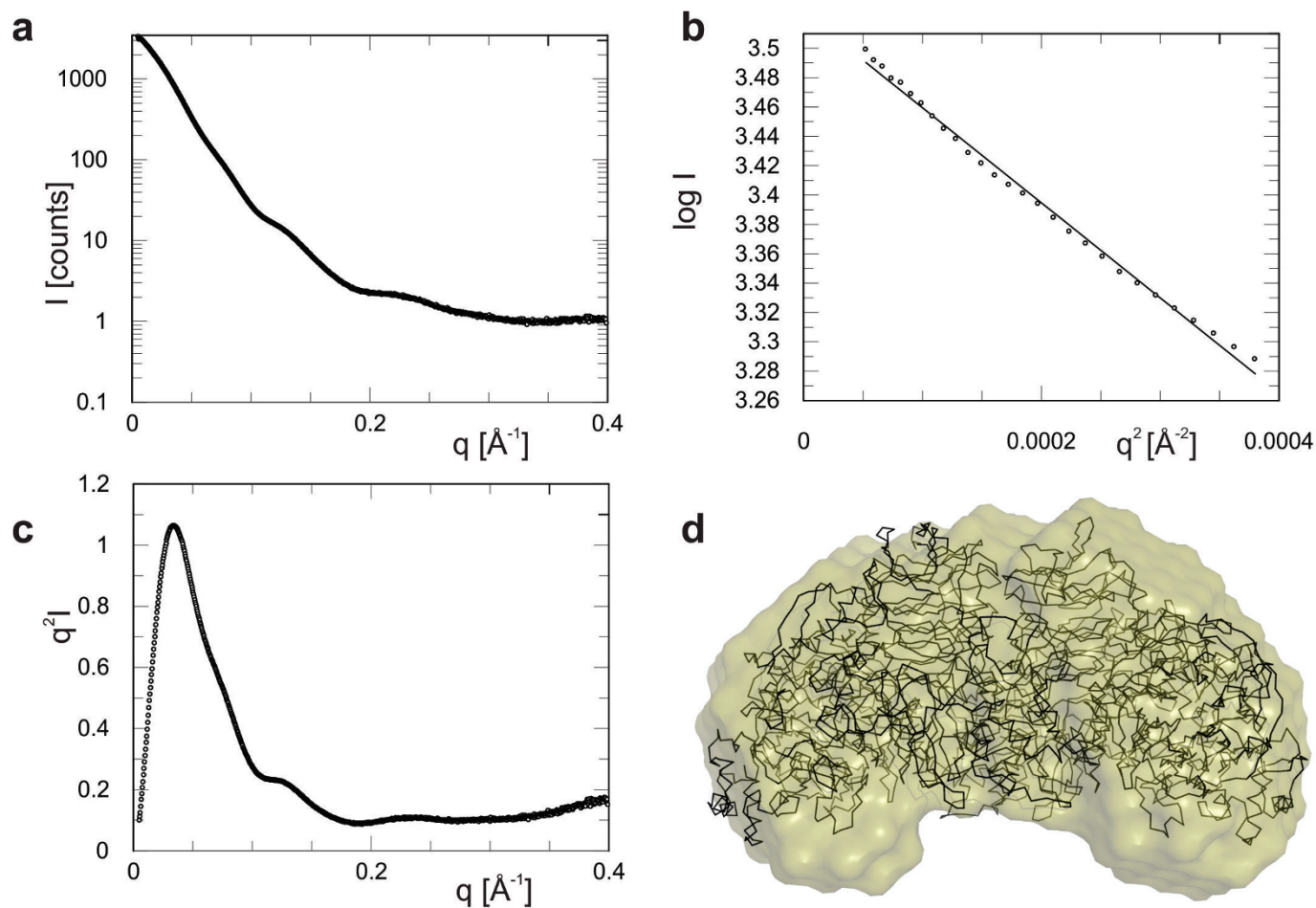
Hanborough, UK) and incubating for 5 min at -20 °C and a xenon pressure of 20 bar before freezing in liquid propane.

X-ray data collection, structure solution and analysis. Diffraction data were collected at beam line X10SA of the Swiss Light Source (Paul Scherrer Institute, Villigen, Switzerland) at 100 K and processed with XDS²⁰. A highly redundant single-wavelength anomalous dispersion (SAD) data set at a resolution of 3.7 Å was collected just above the iron K-edge at a wavelength of 1.735 Å (see Extended Data Table 1) which was used for phase determination with AutoSHARP²¹. SHELXD²² identified 5 heavy atom sites (CC(E) = 0.24), which were used by SHARP for phasing, resulting in a figure-of-merit of 0.22. Density modification with SOLOMON²³ resulted in a readily interpretable map, into which the structures of all three subunits could be built using Coot²⁴. Phase extension using a data set of 3.1 Å collected at 0.9763 Å wavelength was carried out with DM²⁵. Further refinement against a 2.7 Å data set collected at 1.0000 Å wavelength using PHENIX²⁶ and REFMAC²⁷ resulted in a model with good geometry and R-factors (96.4% of residues in favoured regions of the Ramachandran plot, 0.07% Ramachandran outliers, see Extended Data Table 1) and revealed that two loop regions in the α -subunit (α 175–177 and α 643–650) were no longer ordered, despite the increase in overall resolution. In order to confirm the identity of the metal sites, data sets above and below the K-edges of iron, copper and zinc were collected (see Supplementary Information and Extended Data Table 2). All other data-processing procedures were performed with programs of the CCP4 suite²⁸. Tunnels were identified using MOLE 2.0 (ref. 29) using standard parameter settings starting from α Thr571, α Tyr591 and γ Asp168. Structural figures were prepared using Pymol (Schrödinger). The model of the hydroxylamine complex was prepared by manual docking in COOT²⁴, using an iron–nitrogen bond length between haem α I and hydroxylamine as observed in crystal structures of catalase–hydroxylamine complexes.

Small-angle X-ray scattering (SAXS). Hydrazine synthase was concentrated to 45 mg ml⁻¹ in 25 mM HEPES/KOH pH 7.5, 25 mM KCl. SAX data were measured in 1-mm diameter quartz capillaries at the X12SA beam line (cSAXS) of the Swiss Light Source (Paul Scherrer Institute, Villigen, Switzerland) at 283 K. The X-ray photon energy was 12.4 keV, and 200 measurements of 0.5 s each were recorded over 10 positions along the length of the capillary, which was mounted at a detector distance of 2.138 m. Background measurements with the buffer only were taken using the identical capillaries, positions and measurement protocol. Data were used to a maximum momentum transfer of 0.4 Å⁻¹. Data analysis and three-dimensional reconstruction were performed using the GNOM³⁰ and GASBOR³¹ programs from the ATSAS suite.

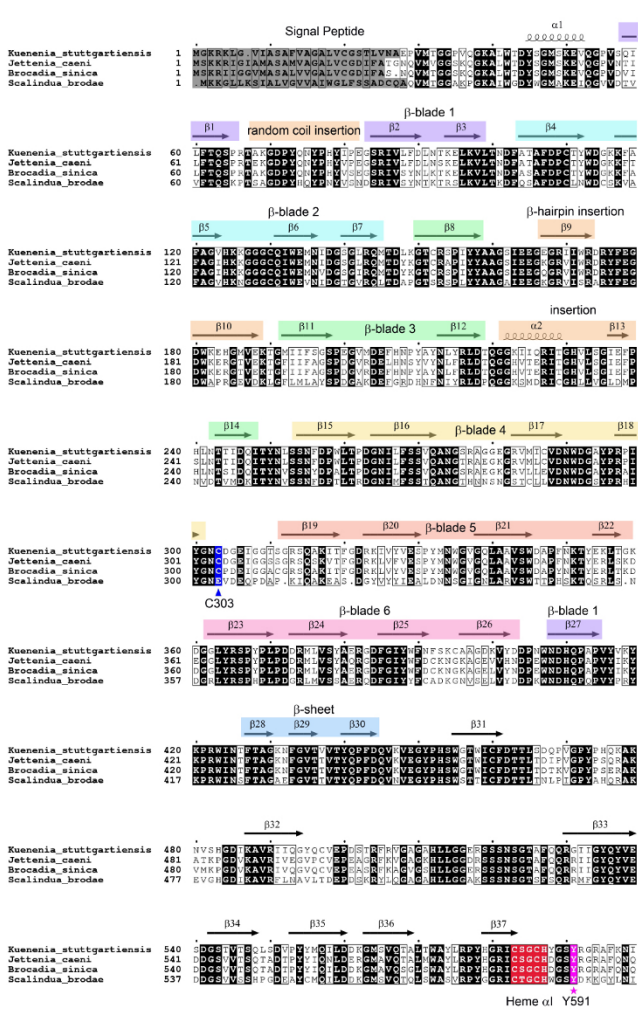
EPR spectroscopy. EPR spectroscopy was performed with a Varian E-9 spectrometer operating at X-band (microwave frequency 9.188 GHz; modulation amplitude, 1.0 mT) equipped with a home-made He-flow cryostat at 12 K. HZS samples were used as isolated at a concentration of 205 μ M, filled into quartz tubes and shock frozen in liquid nitrogen before the measurements. Samples in the presence of 200 μ M NH₂OH or 200 μ M NO plus 200 μ M NH₄⁺ were prepared and analysed in the same way.

- Bendtsen, J. D., Nielsen, H., von Heijne, G. & Brunak, S. Improved prediction of signal peptides: SignalP 3.0. *J. Mol. Biol.* **340**, 783–795 (2004).
- Brown, P. H. & Schuck, P. Macromolecular size-and-shape distributions by sedimentation velocity analytical ultracentrifugation. *Biophys. J.* **90**, 4651–4661 (2006).
- Kabsch, W. XDS. *Acta Crystallogr. D* **66**, 125–132 (2010).
- Vonrhein, C., Blanc, E., Roversi, P. & Brice, G. Automated structure solution with autoSHARP. *Methods Mol. Biol.* **364**, 215–230 (2007).
- Schneider, T. R. & Sheldrick, G. M. Substructure solution with SHELXD. *Acta Crystallogr. D* **58**, 1772–1779 (2002).
- Abrahams, J. P. & Leslie, A. G. W. Methods used in the structure determination of bovine mitochondrial F₁ ATPase. *Acta Crystallogr. D* **52**, 30–42 (1996).
- Emsley, P. & Cowtan, K. Coot: model-building tools for molecular graphics. *Acta Crystallogr. D* **60**, 2126–2132 (2004).
- Cowan, K. D. & Zhang, K. Y. J. Density modification for macromolecular phase improvement. *Prog. Biophys. Mol. Biol.* **72**, 245–270 (1999).
- Adams, P. D. et al. PHENIX: a comprehensive Python-based system for macromolecular structure solution. *Acta Crystallogr. D* **66**, 213–221 (2010).
- Murshudov, G. N., Vagin, A. A. & Dodson, E. J. Refinement of macromolecular structures by the maximum-likelihood method. *Acta Crystallogr. D* **53**, 240–255 (1997).
- Collaborative Computational Project, Number 4. The CCP4 suite: programs for protein crystallography. *Acta Crystallogr. D* **50**, 760–763 (1994).
- Petřek, M., Kosinova, P., Koca, J. & Otyepka, M. MOLE: a Voronoi diagram-based explorer of molecular channels, pores, and tunnels. *Structure* **15**, 1357–1363 (2007).
- Svergun, D. I. Determination of the regularization parameter in indirect-transform methods using perceptual criteria. *J. Appl. Cryst.* **25**, 495–503 (1992).
- Svergun, D. I., Petoukhov, M. V. & Koch, M. H. J. Determination of domain structure of proteins from X-ray solution scattering. *Biophys. J.* **80**, 2946–2953 (2001).
- Pettersen, E. F. et al. UCSF Chimera—a visualization system for exploratory research and analysis. *J. Comput. Chem.* **25**, 1605–1612 (2004).



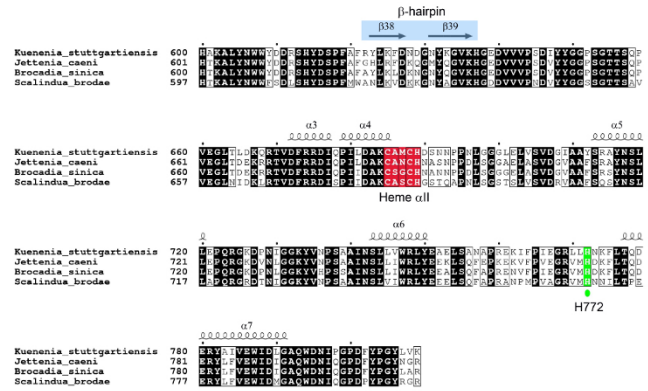
Extended Data Figure 1 | Small-angle X-ray Scattering (SAXS) results. **a**, Semilogarithmic plot of scattered intensity I versus q , which was defined as $q = (4\pi \sin \vartheta)/\lambda$. The curve is an average over 200 measurements. Features are observed up to $q = 0.4 \text{ \AA}^{-1}$. **b**, Guinier plot (plot of $\log I$ versus q^2) showing

that the protein is not aggregated. **c**, Kratky plot (plot of $q^2 I$ versus q) showing that the protein is folded. **d**, Average of 18 (out of 20) dummy-atom reconstructions (beige) overlaid on the crystal structure (black).



6-bladed β-propeller

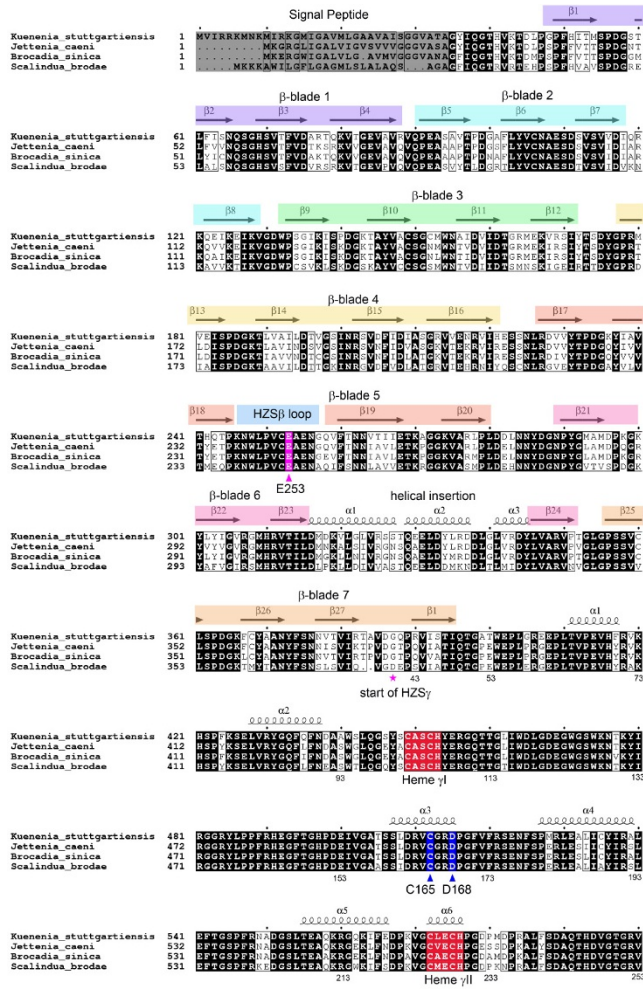
Heme Domain 1



Heme Domain 2

Extended Data Figure 2 | HZS-α sequences. The HZS-α sequences from *Kueneinia stuttgartiensis* (kuste2861, gi 91200564), *Jettenia caeni* (Planctomycete KSU-1, ksu1d0439, tr A9ZRZ5), *Brocadia sinica* JPN1 (brosiA2676, gi 762182098) and *Scalindua brodae* (scabro01598, gi 726045835, re-confirmed by Sanger sequencing) were aligned in ClustalW and secondary structure elements were manually assigned based on the structure of *Kueneinia* HZS-α. Kuste2861 shares 81% sequence identity with its *Jettenia* and

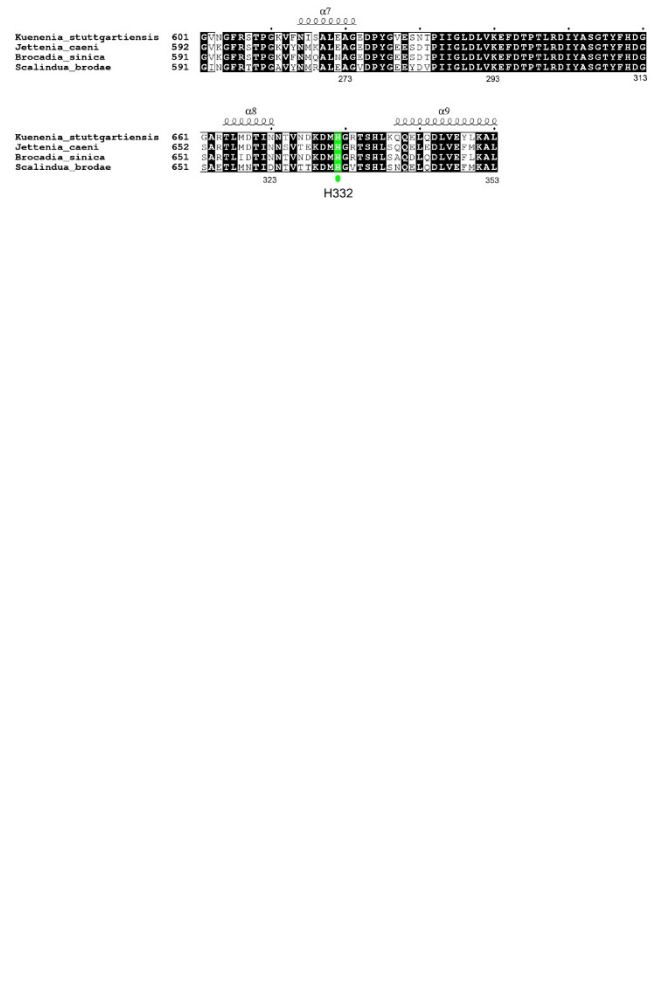
Brocadia orthologues and 61% with *Scalindua*. Fully conserved peptide sequences are marked black. The predicted signal peptides are highlighted in grey. The following residues are marked (numbering according to kuste2861): Cys303 coordinating Zn²⁺ (blue triangle), Tyr591 coordinating haem αI (pink asterisk), distal His772 of haem αII (green circle). The c-type haem binding motifs are highlighted in red. The figure was prepared using ESPript.



7-bladed beta-propeller

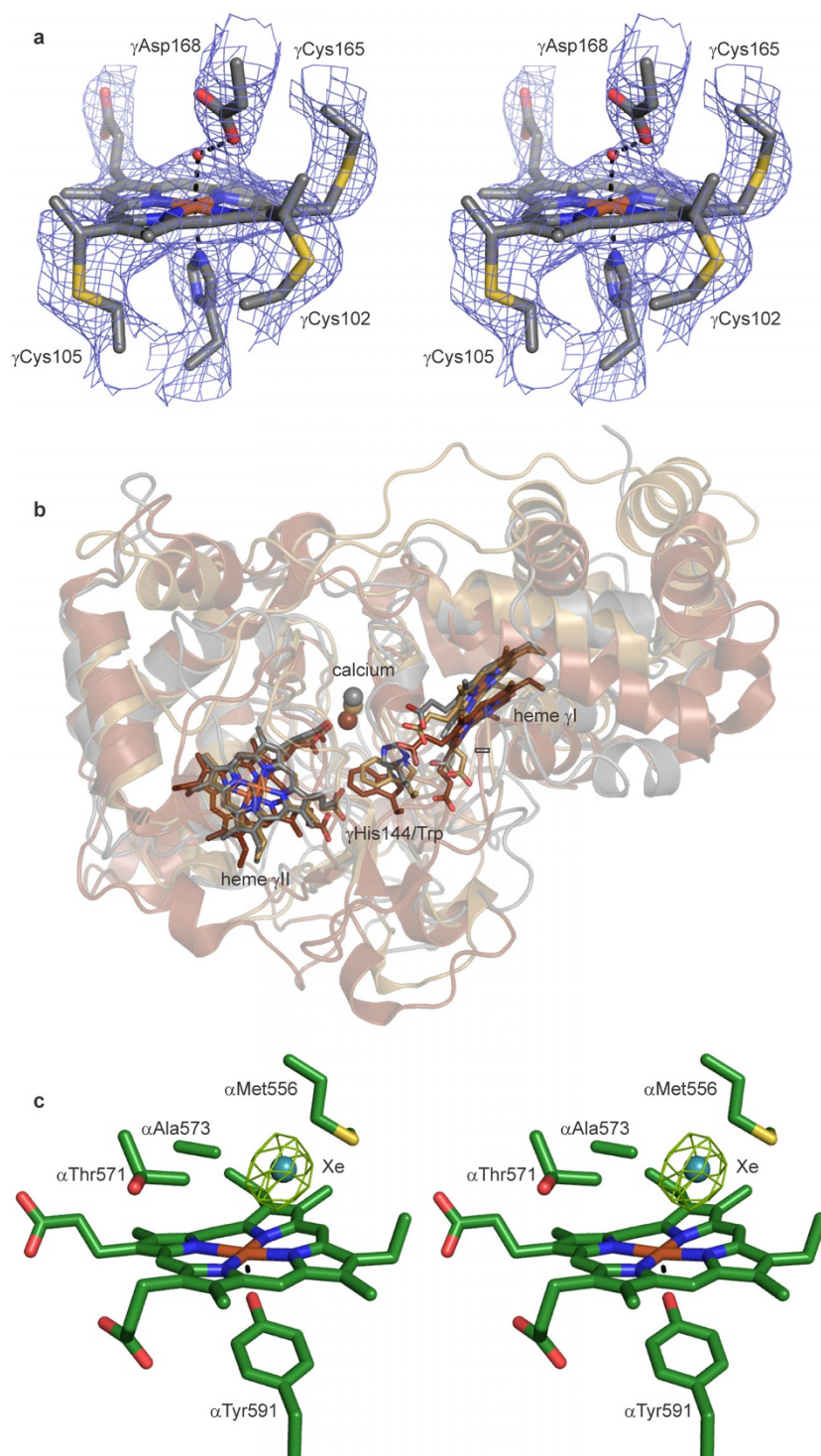
Heme Domain 1

Heme Domain 2



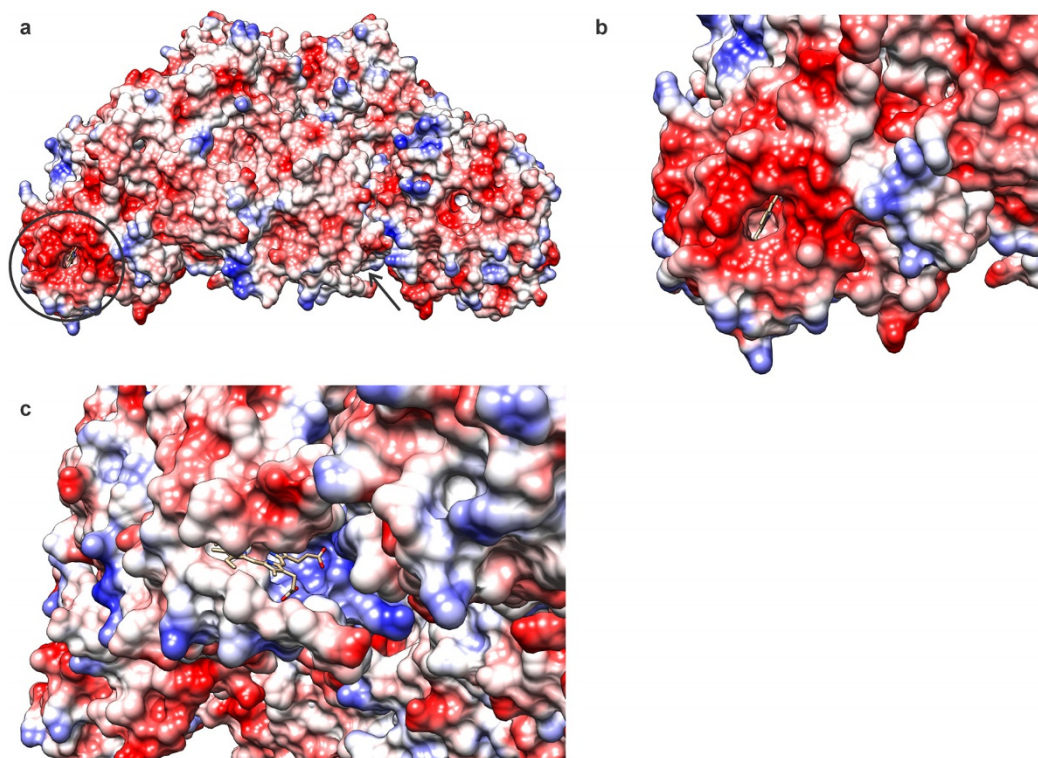
Extended Data Figure 3 | Sequence alignments of HZS- β and HZS- γ . The HZS- $\beta\gamma$ fusion protein from *Scalindua brodae* (scabro01046, gi 726046454, re-confirmed by Sanger sequencing) was aligned using ClustalW to the fused sequences of *K. stuttgartiensis* HZS- β (kuste2859, gi 91200562) and HZS- γ (kuste2860, gi 91200563, lacking its predicted signal peptide) as well as to the fused sequences of *Jettienia caeni* (Planctomycete KSU-1) HZS- β (ksu1d0441, tr I31P5) and HZS- γ (ksu1d0440, tr A9ZRZ4, lacking its predicted signal peptide) and the fused sequences of *Brocadia sinica* JPN1 HZS- β (brosiA2674, gi 762182096) and HZS- γ (brosiA2675, gi 762182097, lacking its predicted signal peptide). Secondary structure elements were manually assigned based on the structures of *K. stuttgartiensis* HZS- β and HZS- γ . The first residue of HZS- γ in the HZS $\beta\gamma$ fusions is indicated by a pink asterisk (starting at residue number 40 of *K. stuttgartiensis* HZS- γ , the numbers under the *Scalindua*

sequence indicate the numbering in kuste2860). The Kuste2859–60 fusion shares 83% sequence identity with its *J. caeni* and *B. sinica* orthologues and 72% with *S. brodae*. Fully conserved peptide sequences are marked in black. The predicted signal peptides of the β -subunits are highlighted in grey. The following residues are marked (numbering according to kuste2859 and kuste2860): Glu253 in HZS- β (pink triangle), Cys165 covalently bound to haem γ I, Asp188 near the haem γ I catalytic site (blue triangle) and the distal His332 of haem γ II (green circle). The c-type haem binding motifs are highlighted in red. The figure was prepared using ESPrInt. The predicted signal peptides of the γ -subunits not included in the alignment are: kuste2860: MAREMRLGGKERMKTGVVKIGLVAALGVVGLISAGGVYA_GQP...; ksu1d0440: MRNGMIKIGLVAALGIAGVVTAGEIMA_GTP...; brosiA2675: MKSSLKIGLIAALGIAGVMTTGELMA_GTP.



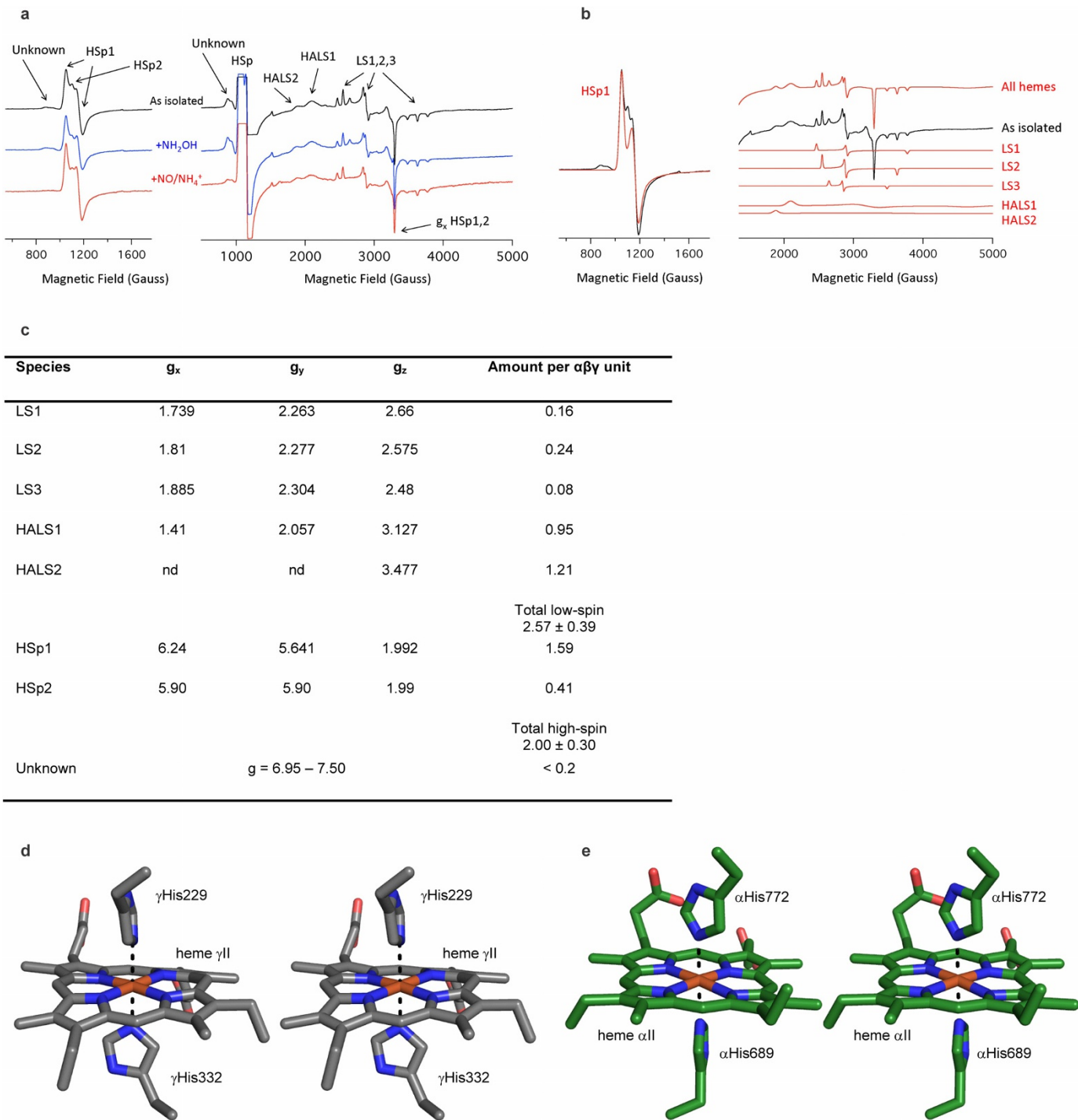
Extended Data Figure 4 | Details of HZS structure. **a**, Covalent attachment of haem γ I via three cysteine sulfur atoms. The simulated annealing $2mF_o - DF_c$ composite omit map is shown contoured at 1σ , overlaid on the final, refined structure. γ Cys102 and γ Cys105 are part of the canonical CXXCH motif (grey cartoon). In addition, there is a covalent bond between the S_γ atom of γ Cys165 and the C_1 porphyrin methyl group of haem γ I. **b**, Overlay of HZS γ (grey) with *N. europaea* CCP (PDB entry 1IQC, light brown) and *P. denitrificans* MauG (PDB entry 3L4M, dark brown). The positions of

haems γ I and γ II correspond to those of the haems in CCP and MauG (sticks), as does the position of a calcium ion (spheres). The conserved tryptophan residue proposed to be involved in redox catalysis in MauG and CCP corresponds to His144 in HZS- γ (sticks). **c**, Xenon binding shows that haem α I is accessible from the solvent. The Xe atom is shown as a sphere. Green mesh: $mF_o - DF_c$ map calculated before inclusion of Xe in the model, (10σ). α Met556 has assumed a new conformation.



Extended Data Figure 5 | Electrostatic surface properties of the HZS complex. Haem moieties are shown as sticks. **a**, Overview of the whole HZS structure. The bis-His-coordinated haem γ II is indicated with a black circle. Haem α II is obscured in this view but its position is indicated by a black arrow. **b**, Magnified view of the electrostatic properties of the surface

surrounding haem γ II. A prominent negatively charged patch surrounds the haem as in cytochrome *c* binding sites. **c**, Magnified view of the vacuum electrostatic properties of the surface surrounding haem α II. No significant differences with the rest of the protein surface are observed. Figure prepared using UCSF Chimera³².



Extended Data Figure 6 | EPR spectroscopy of HZS. **a**, EPR spectra of HZS as isolated (black traces) and after addition of $200 \mu\text{M}$ NH_2OH (blue traces) or $200 \mu\text{M}$ NO plus $200 \mu\text{M}$ NH_4^+ (red traces). The left panel shows the low magnetic field region highlighting the high-spin haem g_x and g_y resonances. The right panel shows the complete magnetic field scan where the intensity of the high-spin haem signals has run off-scale. Arrows indicate the positions of the various species that are listed in Extended Data Fig. 6c. The signal at 1540 Gauss is due to a small amount ($<0.2\%$ per $\alpha\beta\gamma$ unit) of adventitious iron. **b**, Simulation of the EPR spectra of HZS as isolated using the g values listed in Extended Data Fig. 6c. The difference between the simulation of HSp1 and the experimental spectrum defines the signal of HSp2 and its g value and suggests an amount of 0.41 per $\alpha\beta\gamma$ unit (see panel c). **c**, HZS haem content

per $\alpha\beta\gamma$ unit determined by EPR. The total haem content determined by EPR was 0.92 ± 0.15 of the optically determined amount. nd, not detectable; LS, low-spin; HALS, highly anisotropic low-spin; HSp, rhombic high-spin peak. **d**, Stereofigure of the coordination of haem γII by $\gamma\text{His}229$ and $\gamma\text{His}332$. The perpendicular orientation of the histidine imidazole rings, both oriented towards haem *meso* atoms, is consistent with the g -values for HALS2. **e**, Stereofigure of the coordination of haem αII by $\alpha\text{His}689$ and $\alpha\text{His}772$. The orientation of the histidine imidazole groups, one ($\alpha\text{His}772$) oriented towards a haem nitrogen atom and the other ($\alpha\text{His}689$) towards a haem *meso* atom is consistent with the g values for HALS1 (see Supplementary Information).

Extended Data Table 1 | Data collection and refinement statistics

	SAD	Initial Model	Native structure (pdb 5C2V)	Xenon complex (pdb 5C2W)
Data collection[†]				
Space group	<i>R</i> 32	<i>R</i> 32	<i>R</i> 32	<i>R</i> 32
Cell dimensions				
<i>a</i> , <i>b</i> , <i>c</i> (Å)	461.8, 461.8, 145.1	464.0, 464.0, 145.0	464.5, 464.5, 145.8	464.1, 464.1, 145.1
α , β , γ (°)	90, 90, 120	90, 90, 120	90, 90, 120	90, 90, 120
Resolution (Å)	40-3.4 (3.5-3.4) [†]	40-3.1(3.2-3.1)	40-2.7 (2.8-2.7)	48.5-3.2 (3.3-3.2)
<i>R</i> _{merge}	0.103 (0.530)	0.100 (0.498)	0.096 (0.738)	0.138 (0.641)
<i>I</i> / σ <i>I</i>	17.8 (3.2)	16.4 (3.7)	18.5 (3.5)	16.6 (4.6)
Completeness (%)	99.9 (100)	99.8 (99.8)	99.8 (100)	100.0 (100.0)
Redundancy	11.7 (8.1)	5.7 (5.6)	8.8 (9.1)	10.6 (10.8)
Refinement				
Resolution (Å)			40-2.7	48.5-3.2
No. reflections			162,788	97,821
<i>R</i> _{work} / <i>R</i> _{free}			0.235 / 0.271	0.231 / 0.267
No. atoms				
Protein			22,420	22,420
Ligand/ion			344 (8 heme) 18 (12 Ca, 2 Zn, 2 Mg, 2 Cl) 56 (7 betaines)	344 (8 heme) 18 (12 Ca, 2 Zn, 2 Mg, 2 Cl) 56 (7 betaines), 4 Xe
Water			500	498
B-factors (Å ²)				
Protein			56.9	71.0
Ligand/ion			58.3	61.4
Water			53.4	57.4
R.m.s deviations				
Bond lengths (Å)			0.009	0.009
Bond angles (°)			1.2	1.3

*Each data set was collected from a single crystal.

†Highest resolution shell is shown in parentheses.

Extended Data Table 2 | Identification of metals in hydrazine synthase

a

Data set*	Above Fe-edge	Below Fe-edge	Above Cu-edge
Space group	R32	R32	R32
Unit cell dimensions			
<i>a</i> , <i>b</i> , <i>c</i> (Å)	467.2, 467.2, 146.0	465.3, 465.3, 145.5	465.3, 465.3, 145.5
α , β , γ (°)	90, 90, 120	90, 90, 120	90, 90, 120
Wavelength (Å)	1.73400	1.74600	1.37800
Resolution range (Å) †	30.0-3.80 (3.9-3.8)	30.0-3.50 (3.6-3.5)	30.0-3.20 (3.3-3.2)
Reflections measured	1,165,022 (88,940)	1,469,568 (107,411)	1,995,467 (172,227)
Reflections unique	116,983 (8,703)	147,985 (12,027)	193,705 (17,117)
Completeness (%)	99.9 (99.8)	99.9 (100)	100 (100)
Redundancy N	10.0 (10.2)	9.9 (8.9)	10.3 (10.1)
<i>I</i> / σ I	14.4 (4.7)	18.6 (5.2)	22.2 (6.5)
<i>R</i> _{merge} (%)	15.5 (59.7)	12.6 (50.1)	9.5 (43.6)

Data set	Below Cu-edge	Above Zn-edge	Below Zn-edge
Space group	R32	R32	R32
Unit cell dimensions			
<i>a</i> , <i>b</i> , <i>c</i> (Å)	466.0, 466.0, 146.4	465.0, 465.0, 144.6	465.9, 465.9, 145.0
α , β , γ (°)	90, 90, 120	90, 90, 120	90, 90, 120
Wavelength (Å)	1.38500	1.28100	1.29433
Resolution range (Å) †	30.0-3.40 (3.5-3.4)	40.0-3.50 (3.6-3.5)	40.0-3.80 (3.9-3.8)
Reflections measured	1,669,421 (143,426)	1,465,592 (111,737)	1,134,042 (79,076)
Reflections unique	162,603 (13,535)	147,007 (11,917)	115,562 (8,699)
Completeness (%)	100 (100)	99.9 (100)	99.9 (100)
Redundancy N	10.3 (10.6)	10.0 (9.4)	9.8 (9.1)
<i>I</i> / σ I	17.6 (5.6)	15.4 (3.8)	16.2 (4.6)
<i>R</i> _{merge} (%)	13.1 (55.4)	13.3 (68.3)	13.2 (64.1)

b

Element/position wrt. absorption edge	Fe/below	Fe/above	Cu/below	Cu/above	Zn/below	Zn/above
Wavelength (Å)	1.746	1.734	1.385	1.378	1.29433	1.281
Energy (eV)	7101	7150	8952	8997	9579	9679
Energy difference from K-edge (eV)	-11	38	-27	18	-80	20
HZS α						
Ca α I	8.1/1.0	6.5/1.0	6.7/1.0	8.8/1.0	6.0/1.0	4.7/1.0
Ca α II	8.7/1.0	4.2/0.6	5.6/0.8	7.7/0.8	4.7/0.8	3.4/0.7
Zn	8.5/1.0	5.7/0.9	4.2/0.6	7.2/0.8	4.5/0.8	24.3/5.2
Fe Heme α I	4.4/0.5	20.3/3.1	20.5/3.1	27.4/3.1	17.4/2.9	16.3/3.5
Fe Heme α II	3.8/0.5	18.8/2.9	18.5/2.8	23.5/2.7	15.3/2.6	12.6/2.7
HZS β						
Ca β I	8.9/1.1	6.6/1.0	5.8/0.9	7.9/0.9	4.5/0.8	4.3/0.9
HZS γ						
Ca γ I	9.9/1.2	6.0/0.90	8.4/1.3	11.2/1.3	6.5/1.1	4.6/1.0
Ca γ II	8.5/1.0	8.7/1.3	6.8/1.0	8.1/0.9	5.5/0.9	4.6/1.0
Ca γ III	12.2/1.5	8.3/1.3	6.8/1.0	11.2/1.3	7.1/1.2	4.6/1.0
Fe Heme γ I	5.9/0.7	17.5/2.7	20.4/3.0	27.0/3.1	14.0/2.3	13.8/2.9
Fe Heme γ II	5.5/0.7	16.2/2.5	17.6/2.6	23.0/2.6	13.3/2.2	12.9/2.7

a, Data collection statistics for the anomalous diffraction data sets used to identify metal sites in the HZS crystal structure, calculated while considering Friedel mates as individual reflections. *Each data set was collected from a single crystal, †Highest resolution shell is shown in parentheses. b, Heights of peaks in anomalous difference density maps used to identify metal ions. The first number is the observed peak height in σ , the second is the peak height normalized by the height of the anomalous peak at calcium α I for each data set. Those sites that show a significant difference in normalized peak height below and above an absorption edge are shown in grey. The data confirm the identity of the zinc ion bound to haem α I.